Investigation of the role of morphology on the magnetic properties of $Ca_2Mn_3O_8$ materials

Laura J. Vera Stimpson,[a] Silvia Ramos,[a] Gavin B. G. Stenning,[b] Marek Jura,[b] Stephen Parry,[c] Giannantonio Cibin[c] and Donna C. Arnold[a*]

[a] School of Physical Sciences, University of Kent, Canterbury, Kent, CT2 7NH, UK

[b] ISIS Neutron and Muon Source, Rutherford Appleton Laboratory, Harwell Science and Innovation Campus, Didcot, OX11 0QX, UK

[c] Diamond Light Source, Harwell Science and Innovation Campus, Didcot, Oxfordshire OX11 0DE, UK

[*] Corresponding Author, Donna C. Arnold, e-mail: d.c.arnold@kent.ac.uk, tel: 01227 827810

$Ca_2Mn_3O_8$ exhibits a complex layered structure comprised of $Mn_3O_8^{4-}$ layers separated by Ca^{2+} ions. In contrast with the more traditional triangular delafossite layered materials the $Mn_3O_8^{4-}$ layers additionally exhibit an ordered vacancy, which forms a 'bow-tie' like arrangement of the Mn^{4+} ions. We report a comprehensive study of the magnetic properties of a series of $Ca_2Mn_3O_8$ materials with different morphologies. EXAFS and XANES analysis confirm no differences in either manganese environment or oxidation state between materials. Apparent differences in magnetic order from SQUID magnetometry can be rationalised by uncompensated surface spins arising as a result of changes to the surface to volume ratio between morphologies. Furthermore, these data suggest these materials are potentially frustrated in nature of $Ca_2Mn_3O_8$, due to the triangular connectivity of Mn^{4+} spins, with a simple 'spin-up/spin-down' (↑↓) antiferromagnetic model unable to explain the data collected.

Introduction

Delafossite materials with the general formula, ABX_2 (where A is a monovalent cation such as Cu^+ or Ag^+, B is typically a trivalent transition metal such as Mn^{3+} or Fe^{3+} and X is normally O^{2-}) have attracted extensive attention due to their compositional flexibility and interesting physical properties (e.g. magnetic, thermoelectric and optical).[1] Structurally, these materials can be thought of as being related to the cubic rock salt structure whereby the large

size difference in the A and B cations results in them being arranged into separate layers, parallel to the [111] close packed plane of the parent rock-salt structure.[2] The M^{3+} cations in these materials are ordered within the layers to give rise to an equilateral triangular arrangement of the magnetic spins. This triangular arrangement of spins is of particular interest since in materials with antiferromagnetic (AFM) nearest neighbour interactions, the pairwise connectivity between magnetic species cannot be satisfied, resulting in ground state degeneracy and leading to unconventional and novel magnetic phenomena.[3] In addition the combined effects of complex spin arrangements and Jahn-Teller (JT) distortions often results in the emergence of ferroelectric order and thus the potential for multiferroic character.[4] Frustration in delafossites is typically partially lifted by a lowering of the crystal symmetry and the propagation of either a 120^o spin spiral or incommensurate spin order. The prototypical delafossite material, $CuFeO_2$, exhibits two magnetic phase transitions ($T_{N1} \approx 14$ K, $T_{N2} \approx 11$ K) whereby the material first orders as a collinear spin density wave with an incommensurate modulation, followed by a collinear commensurate four sub-lattice (4SL, ↑↑↓↓) ordering.[5] As expected, these magnetic phase transitions are accompanied by structural distortions which reduce the symmetry from rhombohedral to monoclinic, which releases the frustration.[5] $AgFeO_2$ has been shown to exhibit similar behaviour at T_{N1} (≈ 15 K) with the evolution of a spin density wave with a temperature dependent incommensurate modulation. This results in a lowering of the crystal symmetry from rhombohedral, $R\bar{3}m$, to monoclinic, $C2/m$.[6] However, in contrast with $CuFeO_2$, below T_{N2} (≈ 9 K) an elliptical cycloid with an incommensurate propagation vector, which can be described by the inverse Dzyaloshinskii-Moriya function is observed.[6] Proper screw spiral spin structures are observed, on the other hand, for $AgCrO_2$ and $CuCrO_2$.[7,8]

Incorporation of JT active species, such as Mn^{3+}, in the framework (e.g. α-$NaMnO_2$) results in a further distortion of the system, with the symmetry of the parent structure decreased to $C2/m$, as a result of distortions arising from the JT MO_6 bond arrangement.[2] For example, the $t_{2g}^3e_g^1$ electronic configuration of Mn^{3+} induces a cooperative ferro-orbital ordering above room temperature. This promotes the elongated Mn-O bonds to lie along the axis of the dz^2 orbitals and establishes an anisotropic isosceles triangular arrangement of the lattice resulting in a lowering of the symmetry and complex magnetic order.[9] α-$NaMnO_2$ has been reported to exhibit 2D AFM ordering below ≈ 200 K and collinear 3D long range ordering below T_N = 45 K which is accompanied by a magnetoelastic lowering of the symmetry from $C2/m$ to a triclinic structure, whereby the frustration is partially released.[2,9,10]

Similarly, $CuMnO_2$ has been reported to have complex nearest neighbour, J1 and diagonal nearest neighbour, J2 interactions.[11] However, anisotropy of the triangular lattice gives rise to a frustrated square lattice.[11] Again magnetoelastic coupling reduces frustration by lowering the symmetry from $C2/m$ to $C\bar{1}$, resulting in magnetic spins AFM aligned along the $[1\bar{1}0]$ direction and FM aligned along the $[110]$ direction. This corresponds to a collinear AFM order.[11]

$Ca_2Mn_3O_8$ exhibits a similar layered structure comprised of infinite $Mn_3O_8^{4-}$ sheets, with closely packed oxygen layers held together by Ca^{2+} ions (Figure 1).[12,13] In contrast with the delafossite materials, both the A- and B-site cation layers are incomplete with a quarter of the available Mn^{4+} octahedral sites vacant; additionally half the Ca^{2+} sites are also vacant. This leads to a network of ordered vacancies perpendicular to the layers, similar to those observed in kagomé lattices.[14] However, these vacancies are ordered such that they realise a novel 'bow tie' connectivity of the Mn^{4+} ions which is distinct from kagomé connectivity as shown in figure 1(b). The location of this vacancy alternates between subsequent $Mn_3O_8^{4-}$ sheets giving rise to ABAB stacking in the lattice a-direction. Since the triangular connectivity of the 'bow-tie' arrangement should be expected to give rise to frustration, it is not unreasonable to expect complex magnetic ordering in these materials. Furthermore, the ordered arrangement of the framework vacancy results in inequivalent Mn^{4+} crystallographic sites which will further influence magnetic order. Despite the potential of these materials for exotic magnetic order, interest in $Ca_2Mn_3O_8$ has been primarily focused on potential catalytic[15-19] and battery[20] applications; the magnetic properties have been largely ignored since the first structural reports in the 1980's.[12,13,21]

In order to gain an understanding of the magnetic behaviour of $Ca_2Mn_3O_8$ we have prepared materials using a number of synthetic methods. Since particle size and morphology of a material can have direct implications on the magnetic properties, we have performed an in-depth characterisation of these materials. Interestingly, different synthetic routes lead to materials which have very different morphologies, ranging from nano-flakes to much larger spherical particles. EXAFS experiments demonstrate that there are no variations in either manganese oxidation state or environment as a result of synthetic method. Comparative SQUID magnetometry measurements demonstrate that perceived differences in the magnetic behaviour can be rationalised by changes in the surface to volume ratio. Furthermore, whilst all materials can be characterised as exhibiting antiferromagnetic order, these comparisons

demonstrate that the order is far more complex than a simple 'spin-up/spin-down' (↑↓) order, consistent with the proposed frustrated nature expected for $Ca_2Mn_3O_8$.

Experimental

Polycrystalline $Ca_2Mn_3O_8$ samples were prepared using sol-gel, hydrothermal and co-precipitation synthetic methods. Sol-gel samples were prepared using the method reported by Park et al.[20] Briefly, stoichiometric ratios of $Mn(CH_3CO_2)_2.4H_2O$ and $Ca(NO_3)_2.4H_2O$ (both Aldrich ≥ 99 %) were dissolved in 10 mL of deionised water. Glycolic acid was added in order to achieve a molar ratio of glycolic acid to metal ions of 2:1. A 1 M solution of ammonium hydroxide was used to increase the pH to > 8. The resulting solution was heated at 80 ^oC until a viscous pink gel was formed. The product was then firstly heated for 5 hours at 450 ^oC (ramp rate 1 ^oC/min), during which the product underwent a vigorous exothermic reaction, followed by a second heating for 5 hours at 750 ^oC (ramp rate 5 ^oC/min) under flowing O_2.

Hydrothermal materials were prepared using a similar method to that reported previously by Arnold et al. for the synthesis of $CaMn_2O_4$ nanowires.[22] Stoichiometric ratios of $Ca(NO_3)_2.4H_2O$, $MnCl_2$ and $KMnO_4$ (Aldrich, ≥ 99 %) with a ratio of 0.7:0.3 for the $MnCl_2$ and $KMnO_4$ precursors respectively, were dissolved in 30 mL of deionised water. KOH was added in order to achieve a highly alkaline solution (pH ≈ 14). The solution was then placed into a 45 mL teflon lined autoclave and heated to 180 ^oC (ramp rate 5 ^oC/min) for 48 hours.

Finally, $Ca_2Mn_3O_8$ was prepared via a co-precipitation method.[13] Firstly manganese carbonate, $MnCO_3$, was freshly precipitated from a manganese nitrate solution, with a 30 % excess of ammonium carbonate. This was dried in a vacuum oven, at 100 ^oC for 12 hours before use. A 2:3 molar ratio of $CaCO_3$ to $MnCO_3$ were dissolved in 100 mL of deionised water followed by the addition of HNO_3 (2.5 M) until a pH of < 5 was observed. This precursor solution was added slowly, with stirring, to a second 100 mL solution containing $(NH_4)_2CO_3$ in water. The resulting precipitate was dried and heated at 700 ^oC (ramp rate 10 ^oC/min) under flowing oxygen for 1 hour.

Phase purity was determined using a Rigaku SmartLab rotating anode θ/2θ diffractometer using Cu Kα radiation (λ = 1.5418 Å) at 45 kV and 200 mA. Rietveld refinements were performed to obtain structural information using the GSAS suite of programs.[23,24] Full details of the refinements performed are given in the electronic supplementary information (ESI).[†] Extended X-ray absorption fine structure (EXAFS) measurements were performed using the B18 beamline at Diamond Light Source, UK.[25] Absorption spectra were collected at room

temperature with transmission geometry at the Mn K-edge (6539 eV) using the Si(111) crystals in the monochromator and the continuous acquisition mode (QuickEXAFS). Data were collected over an energy range of 6339 eV to 7620 eV, using a step size of 0.3 eV. Scanning electron microscopy (SEM) images were obtained using a Hitachi S-3400N SEM instrument. Images were collected under vacuum conditions with a 15 kV electron accelerating voltage. Transmission electron microscopy images were obtained using a Jeol 1230 high contrast transmission electron microscope operating at 80 kV and a Gatan Multiscan digital camera model 791. High magnification SEM images were collected using a Hitachi S-4700 cold field emission SEM instrument with an accelerating voltage of 20 kV. DC magnetic susceptibility measurements were collected using a Magnetic Property Measurement System (MPMS) XL-7 instrument under both zero field cooled (ZFC) and field cooled (FC) environments with an applied magnetic field (H) of 0.1 T between 2 and 300 K. Hysteresis data were collected at 2 K and 300 K in a field range of -7 T to 7 T. AC susceptibility measurements were performed using a PPMS-9 Physical Property Measurement system. Data were collected at fixed frequencies of 100 Hz, 215 Hz, 464 Hz, 1000 Hz, 2154 Hz and 2642 Hz in an applied field of 0.1 T over a temperature range of 2 – 100 K. Physisorption measurements were performed using a Thermoscientific Surfer gas absorption porosimeter. Data were collected using N_2 at 80 K. Prior to these measurements all materials were degassed at 353 K for 12 hours.

Results and Discussion

X-ray diffraction patterns collected for the $Ca_2Mn_3O_8$ materials are shown in figure 2. All materials can be readily indexed to the layered, $Ca_2Mn_3O_8$ structure with monoclinic, C2/m, symmetry. Additionally, a small amount of Mn_2O_3 (≈ 1 %) is observed in the pattern obtained for the hydrothermal material. All materials were refined using the GSAS suite of programs and showed good agreement with the model proposed by Ansell et al.[12], as shown in figure 1(b) for the sol-gel prepared material and the ESI for the hydrothermal and co-precipitation materials respectively.[†] Comparison of the cell parameters (Table 1) indicates very little variation across all preparatory methods confirming that synthetic route has little effect on the phase adopted by these materials. A full summary of the refined parameters are given in the ESI.[†]

In all cases the materials exhibited low intensity broad Bragg peaks which can be suggestive of either nanocrystalline morphology or possible strain effects within these

materials. In the Rietveld refinements the peak shape was described using the pseudo-Voigt method which employs a multi-term Simpson's rule for the integration of the function.[26,27] Using this methodology we are able to effectively probe the Gaussian (GU, GV, GW) and Lorentzian (LX, LY) terms independently. Of particular interest are the Lorentzian terms which, within this function, describe peak broadening arising as a result of strain (LY) and crystallite size (LX). It is clear from the refinements for the materials prepared by sol-gel and hydrothermal methods that both strain and crystallite size contribute to the broadening of the Bragg peaks, suggesting that these materials are indeed nanostructured. In contrast, the refinement for the material prepared by the co-precipitation method suggests that strain broadening does not contribute to the broadening of the Bragg peaks, with the LY term consistently refining to zero. When considering peak broadening arising from crystallite size it is important to consider that crystallite size does not necessarily describe particle size. For example crystallites within a material can be thought of as grains separated by grain boundaries and forming much larger particles. In this context crystallite size peak broadening can be defined as arising from either nanostructured single domain particles or from larger particles which are comprised of multiple nano-sized crystalline domains. If we further consider the effects of nano-sized materials it can be suggested that the geometry of nanoparticles also results in the materials experiencing some degree of strain imposed by particle size constraints. The absence of a strain term in the $Ca_2Mn_3O_8$ material formed by co-precipitation methods would therefore, seem to suggest that whilst crystallite size is in the nano regime, giving rise to the observed peak broadening, that the particle size may be much larger minimising the effects of strain.

Bond lengths and bond angles (ESI) † are consistent with those proposed by Ansell et al.[12] A small amount of variation can be seen across the three synthetic methodologies, likely to arise as a result of strain effects (due to the different morphologies) and as a result of limitations in the data quality impeding full refinement of atomic positions; especially since the determination of the atomic position of lighter elements such as oxygen can be difficult. However, these data demonstrate that the synthesis route has very little effect on the structure.

In order to further investigate sample morphology electron microscopy studies were undertaken. It was clear from both low resolution (SEM) and high resolution (FE-SEM, TEM) studies that the morphology is critically dependent on the synthetic approach adopted (Figure 3). Sol-gel synthesis yields agglomerated $Ca_2Mn_3O_8$ nanoparticles with an average diameter of approximately 60 nm and a specific surface area of 21 – 22 m^2/g (as determined

by physisorption measurements). In contrast hydrothermal synthesis results in particles with a flake-like morphology. The diameter of these flakes is large, ~0.8 μm with thicknesses of ≤ 20 nm. BET measurements gave a slightly larger specific surface area of 28 – 31 m^2/g, when compared with the sol-gel prepared $Ca_2Mn_3O_8$ materials consistent with the large flake-like morphology. Co-precipitation methods yield microspheres with a wide size distribution, ranging between 1.2 μm and 4.2 μm consistent with the observations of larger particle sizes from X-ray diffraction. This confirms that the peak broadening arises as a result of the formation of much smaller crystallites within the larger spheres. This may be as a result of the loss of carbon as CO_2 from the material during synthesis which prevents the material forming larger crystallites. Porosity measurements confirm a larger surface area of 31 – 34 m^2/g, when compared to materials synthesised by both hydrothermal and sol-gel methods.

We further investigated the effects of the synthetic method on the local manganese environment in these materials by performing X-ray absorption spectroscopy measurements. Analysis of the XANES region at the Mn K-edge confirmed an average manganese oxidation state of +4 irrespective of synthetic method, consistent with the proposed model (Figure 4).[12] The extended X-ray absorption fine structure (EXAFS) part of the spectrum was also analysed for each of the materials prepared by the three synthetic routes. The same model was used to fit all three samples, confirming that the local structure is also consistent with a single structure obtained for all three materials. As can be seen in the example shown in figure 5, which shows the fitted data for the sol-gel sample, the fit reproduces very closely the data up to radial distance of 3.44 Å from the Mn site. Comparisons between the data for all three materials and fits for the hydrothermal and co-precipitation synthesised materials can be found in the ESI.† Note that in order to minimise the number of free parameters in the fit, a single Mn site was considered rather than the two that the diffraction refinement suggests. The distortion in these two MnO_6 octahedra is sufficiently small so that a regular octahedron can be used to model the data (see Table 2). However, the relatively low value of the S_o parameter (significantly smaller than the ideal value of 1) and the large value of the Debye-Waller factor for the Mn-Ca distances suggest a slight deviation from this ideal structure (consistent with the results from the diffraction measurements). The only significant difference in the structure for the three samples is that a slightly higher value of the Debye-Waller terms is observed for the sample obtained by hydrothermal synthesis, which indicates this sample is more disordered than the other two. Whilst, this is consistent with the larger specific surface area measured for this flake-like material it may also arise as a result of the small amount of Mn_2O_3 impurity phase present in this material.

Magnetic susceptibility data collected for these materials show some marked differences between synthetic routes as shown in figure 6. $Ca_2Mn_3O_8$ prepared by the co-precipitation method shows a broad antiferromagnetic phase transition consistent with that previously reported by Horowitz et al.[12,13] suggestive of low dimensional and/or frustrated magnetic order. This is not unusual in materials which exhibit layered or triangular lattices as observed by Giot et al. for the delafossite, α-$NaMnO_2$ material.[4] The Neél temperature (T_N) was extracted from the derivative, d(χT)/dT, and determined to be approximately 60 K with the Weiss constant, θ_{CW} determined from $1/\chi$ vs T as -105.5 K further confirming antiferromagnetic character (see ESI).† A slight deviation between Zero Field cooled (ZFC) and Field cooled (FC) data is observed below approximately 40 K which may be suggestive of either low temperature weak ferromagnetic ordering or spin glass/disordered behaviour. The antiferromagnetic transition appears less pronounced in both the hydrothermal and sol-gel prepared $Ca_2Mn_3O_8$ materials. Furthermore, as the surface to volume ratio increases (co-precipitation > sol-gel > hydrothermal) the materials take on an increasingly spin glass-like behaviour. Determination of T_N and θ_{CW} for these materials are shown in table 3. Interestingly all parameters are reasonably consistent with only a small variation as a result of synthetic method. Additionally, all materials show a deviation from Curie-Weiss like behaviour at approximately 130 K. This behaviour is common in these types of layered materials whereby there is the potential to form 1D and 2D spin ordered states before forming a fully ordered 3D Neél state.[4] We note that in the d(χT)/dT plots for both the sol-gel and hydrothermally synthesised materials that the 130 K transition is particularly well pronounced which may suggest that the larger surface:volume ratio exhibited by these materials results in more dominant 1D/2D ordering.

The calculated magnetic moment was determined from the paramagnetic region of the data (200 K – 300 K) using equation 1.

$$C = \frac{N\mu_{calc}^2\mu_B^2}{3k_B} \quad -(1)$$

where C is the Curie constant as determined from the slope of $1/\chi$ vs T, N is Avagadro's number, k_B is the Boltzman constant, μ_B is the Bohr magneton and μ_{calc} is the calculated magnetic moment. This magnetic moment can be compared with the effective magnetic moment, μ_{eff} calculated using equation 2. However, equation 2 gives the effective magnetic moment for a single magnetic ion per formula unit. In this instance there are three manganese

ions per formula unit ($Ca_2Mn_3O_8$) and thus in order to be able to compare the observed magnetic moment derived from our data with the expected magnetic moment we need to further calculate the effective magnetic moment using equation 3.

$$\mu_{eff} = g\sqrt{S(S+1)} \quad -(2)$$

$$\mu_{eff} = g\sqrt{\sum_i (\mu_S)^2} \quad -(3)$$

where S is the sum of the spin quantum numbers of the individual unpaired electrons, μ_{eff} is the effective magnetic moment, g is the Landé factor (g can be taken as 2.0 for spin only moment in transition metals) and i is the number of magnetic ions per formula unit. For all materials good agreement is observed between μ_{eff} and μ_{calc} confirming that there is no significant deviation from Mn^{4+} consistent with the XANES data discussed above. The observed differences in the magnetometry data with changing synthetic methodology can, therefore, not be attributed to variations in oxidation state between materials.

Field dependent measurements (Figure 7) did not show any significant hysteresis at 2 K for any of the materials suggesting that there is no low temperature ferromagnetic/ferrimagnetic behaviour. The possibility of spin glass character was further investigated by collecting variable frequency AC susceptibility data. In all cases no frequency dependence was observed (see ESI).[†] This would seem to rule out the possibility of an antiferromagnetic → spin glass transition at low temperature. In previous studies on antiferromagnetic nanomaterials surface to volume ratio has been shown to lead to uncompensated surface spins which results in the observation of ferromagnetic ordering.[22] It is likely that uncompensated spins are also the origin of the anomalous behaviour observed here. In all materials an antiferromagnetic transition is observed at approximately 60 K, albeit weak in the case of the hydrothermal material. However, the absence of ferromagnetic character is clear from the lack of hysteresis with the data more consistent with the uncompensated surface spins appearing disordered. This would suggest that the spin order in these materials is far more complex than a simple 'spin up/spin down' (↑↓) antiferromagnetic arrangement. Since these materials exhibit a complex triangular topography of interconnected Mn-Mn 'bow-ties' it is conceivable that these materials may exhibit some degree of geometric frustration which may manifest as the apparently disordered surface spin state observed for these materials. The frustration index, f, of a material can be used to determine the potential for frustration

(Equation 4) where a value of 1 can be considered to be indicative of non-frustrated magnetic order whilst the higher the value of f the higher the potential for frustration.[28,29]

$$f = \frac{-\theta_{CW}}{T_N} \quad -(4)$$

The frustration index was determined to be close to 2 for these materials and whilst caution should be exercised as using f as a direct measure of frustration, as it can be affected by both local interactions and dimensionality, it can be suggested that given the topography of these materials some level of frustration is likely.[30] Previously, complex magnetic order has been reported in related delafossite materials including incommensurate ordering; these materials exhibit a layered structure with 2D triangular connectivity of the magnetic cations. Frustration in these types of materials is typically relieved by the adoption of more complex spin-states. For example $CuFeO_2$ exhibits a collinear spin density wave with an incommensurate modulation at T_{N1} with collinear commensurate four sub-lattice (4SL, ↑↑↓↓) ordering at T_{N2}.[5] On the other hand α-$NaMnO_2$ exhibits complex magnetic behaviour whereby the material exhibits a ground state inhomogeneity on the nanoscale with the Néel order the result of local symmetry-breaking pinning sites.[31] It is therefore not inconceivable that the magnetic order of $Ca_2Mn_3O_8$ is also far more complex than a simple antiferromagnetic arrangement in order to relieve frustration. It is clear from our data that this complexity becomes more apparent for high surface to volume ratio morphologies where uncompensated spins appear disordered at the surface of these materials. Unfortunately, the poor crystallinity of these current materials make them unsuitable for magnetic structure determination but clearly further work is required to fully understand the exciting magnetic behaviour in these materials.

Conclusion

We have presented a systematic study of the effects of synthetic method on the morphology of $Ca_2Mn_3O_8$ materials. It is clear that synthetic route plays a key role in the morphology obtained, as would be expected. Hydrothermal synthesis leads to the formation of particles with flake-like geometries and large surface to volume ratios. In contrast sol-gel synthesis leads to the formation of small uniform nanoparticles with co-precipitation methods leading to materials comprised of much larger microspheres. Understanding morphology is important if we are to exploit these materials as catalysts or in battery technologies as have previously

been reported.[16,17,20] Most importantly we have used these varied morphologies to probe the complex magnetic behaviours of these materials. $Ca_2Mn_3O_8$ orders antiferromagnetically with a Néel temperature of approximately 60 K. However, SQUID magnetometry of the materials with high surface to volume ratios shows an apparently disordered surface spin state. Field and frequency dependent data has allowed us to rule out weak ferromagnetism or ferrimagnetism and glass-like behaviour. These data coupled with the potential for a frustrated topology would seemingly suggest that the antiferromagnetically ordered state is far more complex than a simple 'spin-up/spin-down' (↑↓) arrangement. Further magnetic characterisation of these materials is hampered by the formation of small crystallites in the large bulk spheres formed by co-precipitation methods. This leads to broad low intensity diffraction peaks making the material unsuitable for more focussed magnetic structure measurements such as powder neutron diffraction. However, it is clear from these data that $Ca_2Mn_3O_8$ is a potentially exciting material which may offer a new frustrated topology to investigate non-convention magnetic order and new Physics if suitable bulk materials can be prepared.

Acknowledgements

The authors are grateful for the award of an EPSRC DTA studentship (LJV) and for the award of beamtime at the Diamond Light Source, B18 (proposal SP12777-1). We are thankful for access to the Materials Characterisation laboratories at the ISIS Muon and Neutron Source. We also thank Dr Mark Price for assistance with the FE-SEM images and Ian Brown in the School of Biosciences at the University of Kent for access to and assistance collecting TEM data.

Notes and References

† Electronic Supplementary Information (ESI) available: Supplementary information includes full details of all GSAS refinements performed on the powder X-ray diffraction data including full refinement profiles and refinement data. Additional EXAFS data fits and comparisons for the materials not shown in the main body of the text and further supporting data for the magnetic characterisation are also provided. See DOI: 10.1039/c000000x/

1 A. P. Amrute, Z. Lodziana, C. Mondelli, F. Krumeich and Perez-Ramirez J., Chem. Mater., 2013, **25**, 4423.

2 A. M. Abakumov, A. A. Tsirlin, I. Bakaimi, G. Van Tendeloo and A. Lappas, Chem. Mater., 2014, **26**, 3306.

3 C. Stock, L. C. Chapon, O. Adamopoulos, A. Lappas, M. Giot, J. W. Taylor, M. A. Green, C. M. Brown and P. G. Radaelli, Phys. Rev. Lett., 2009, **103**, 077202.

4 M. Giot, L. C. Chapon, J. Androulakis, M. A. Green, P. G. Radaelli and A. Lappas, Phys. Rev. Lett., 2007, **99**, 247211.

5 N. Terada, D. D. Khalyavin, P. Manuel, T. Osakabe, P. G. Radaelli and H. Kitazawa, Phys. Rev. B., 2014, **89**, 220403.

6 N. Terada, D. D. Khalyavin, P. Manuel, Y. Tsujimoto, K. S. Knight, P. G. Radaelli, H. S. Suzuki and H. Kitazawa, Phys. Rev. Lett., 2012, **109**, 097203.

7 M. Soda, K. Kimura, T. Kimura and K. Hirota, Phys. Rev. B., 2010, **81**, 100406.

8 S. Seki, Y. Onose and Y. Tokura, Phys. Rev. B., 2010, **81**, 100406.

9 C. Vecchini, M. Poienar, F. Damay, O. Adamopoulos, A. Daoud-Aladine, A. Lappas, J. M. Perez-Mato, L. C. Chapon and C. Martin, Phys. Rev. B., 2010, **82**, 094404.

10 N. Terada, Y. Tsuchiya, H. Kitazawa, T. Osakabe, N. Metoki, N. Igawa and K. Ohoyama, Phys. Rev. B., 2011, **84**, 064432.

11 F. Damay, M. Poienar, C. Martin, A. Maignan, J. Rodriquez-Carvajal, G. Andre and J. P. Doumerc, Phys. Rev. B., 2009, **80**, 094410.

12 G. B. Ansell, M. A. Modrick, J. M. Longo, K. R. Poeppelmeier and H. S. Horowitz, Acta. Crystallogr. B., 1982, **28**, 1795.

13 H. S. Horowitz and J. M. Longo, Inorg. Chem., 1983, **22**, 73.

14 J. L. Atwood, Nature, 2002, **294**, 1495.

15 X. Han, T. Zhang, J. Du, F. Cheng and J. Chen, Chem. Sci., 2013, **4**, 368.

16 M. M. Najafpour and N. Pashaei S., Dalton Trans., 2012, **41**, 4799.

17 M. M. Najafpour and D. J. Sedigh, Dalton Trans., 2013, **42**, 12173.

18 E. Braktash, I. Zaharieva, M. Schroder, C. Goebel, H. Dau and A. Thomas, Dalton Trans., 2013, **42**, 16920.

19 A. Ramirez, P. Bogdanoff, D. Friedrich and S. Fiechter, Nano Energy, 2012, **1**, 282.

20 Y. J. Park and M. A. Doeff, Solid State Ionics, 2006, **177**, 893.

21 T. R. White, W. S. Glaunsinger, H. S. Horowitz and J. M. Longo, J. Solid State Chem., 1979, **29**, 205.

22 D. C. Arnold, O. Kazakova, G. Audoit, J. M. Tobin, J. S. Kulkarni, S. Nikitenko, M. A. Morris and J. D. Holmes, Chem. Phys. Chem., 2007, **8**, 1694.

23 A. C. Larson and R. B. von Dreele, Los Alamos National Report LAUR, 1994, **96**, 86.

24 B. H. Toby, J. Appl. Crystallogr., 2001, **34**, 210.

25 A. J. Dent, G. Cibi, S. Ramos, A. D. Smith, S. M. Scott, L. Varandas, M. R. Pearson, N. A. Krumpa, C. P. Jones and P. E. Robins, J. Phys: Conference Series, 2009, **190**, 012039.

26 C. J. Howard, J. Appl. Crystallogr., 1982, **15**, 615.

27 P. Thompson, D. E. Cox and J. B. Hastings, J. Appl. Crystallogr., 1987, **20**, 79.

28 C. Yin, G. Li, W. A. Kockelmann, F. Liao, J. P. Atfield and J. Lin, Chem. Mater., 2010, **22**, 3269.

29 A. P. Ramirez, Annu. Rev. Mater. Sci., 1994, **24**.

30 A. S. Wills, N. P. Raju, C. Morin and J. E. Greedan, Chem. Mater., 1999, **11**, 1936.

31 A. Zorko, O. Adamopoulos, M. Komelj, D. Arcon and A. Lappas, Nature Commun., 2014, **5**, 3222.

List of Tables

Table 1: Comparison of the lattice parameters determined by Rietveld refinement of the $Ca_2Mn_3O_8$ materials prepared by sol-gel, hydrothermal and co-precipitation methods using the model proposed by Ansell et al.[12]

Parameter	**Ansell Model (ref [12])**	**$Ca_2Mn_3O_8$ Synthetic Method**		
		Sol-gel	**Hydrothermal**	**Co-precipitation**
wRp (%)	-	6.67	4.68	8.59
Rp (%)	-	5.28	3.67	6.80
a (Å)	11.014	11.059(2)	11.023(1)	11.037(1)
b (Å)	5.851	5.8605(9)	5.8537(7)	5.8452(6)
c (Å)	4.942	4.9560(7)	4.9613(4)	4.9505(5)
β (º)	109.73	109.78(1)	109.662(8)	109.752(8)
Cell Volume (Å^3)	299.78	302.26(8)	301.46(5)	300.59(5)

Table 2: Summary of the results obtained for the EXAFS fits for $Ca_2Mn_3O_8$ materials prepared by sol-gel, hydrothermal and co-precipitation methods. Note that statistically there are 16 independent points in the data fitted and 12 parameters used.

Parameter	$Ca_2Mn_3O_8$ Synthetic Method			Interatomic distances taken from the Ansell model (Ref [12])
	Sol-gel	Hydrothermal	Co-precipitation	
S_o	0.65(5)	0.65(6)	0.67(5)	-
E_o (eV)	-3.0(8)	-3(1)	-3.0(8)	-
R Mn1-O1 (Å)	1.893(6)	1.893(8)	1.891(7)	1.902
σ^2 Mn1-O1 (Å^2)	0.004(1)	0.005(1)	0.004(1)	-
R Mn1-Mn2 (Å)	2.899(8)	2.889(9)	2.900(9)	2.899
σ^2 Mn1-Mn2 (Å^2)	0.005(1)	0.005(1)	0.005(1)	-
R Mn1-Ca1 (Å)	3.22(5)	3.2(1)	3.22(4)	3.401
σ^2 Mn1-Ca1 (Å^2)	0.01(1)	0.02(2)	0.010(6)	-
R Mn1-O3 (Å)	3.58(5)	3.58(7)	3.58(4)	3.651
σ^2 Mn1-O3 (Å^2)	0.002(4)	0.003(6)	0.002(4)	-
R Mn1-Ca2 (Å)	3.77(7)	3.74(9)	3.78(8)	-
σ^2 Mn1-Ca2 (Å^2)	0.01(1)	0.02(1)	0.02(1)	-
R-factor	0.007	0.01	0.008	-

Table 3: Magnetic parameters determined from the SQUID magnetometry data collected for $Ca_2Mn_3O_8$ materials prepared by sol-gel, hydrothermal and co-precipitation methods.

Parameter	$Ca_2Mn_3O_8$ Synthetic Method		
	Sol-gel	Hydrothermal	Co-precipitation
T_N (K)	50	50	60
θ_{CW} (K)	-101.9	-102.3	-105.5
μ_{calc} (μ_B)	6.7	6.9	6.4
μ_{eff} (μ_B)	6.7	6.7	6.7
Frustration Index	2.0	2.0	1.8

List of Figures

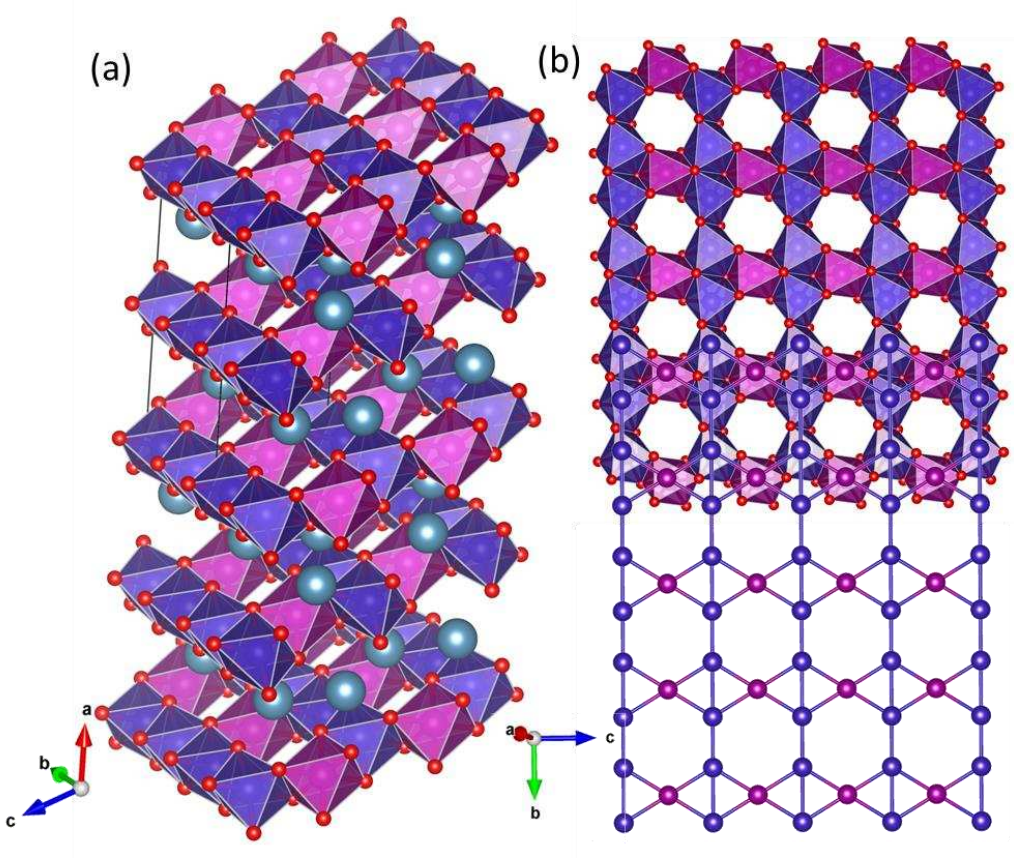

Figure 1: Crystal structure of $Ca_2Mn_3O_8$ (space group: C2/m), where (a) shows the layers formed in the crystallographic a direction and (b) shows the edge shared MnO_6 octahedral network forming ordered vacancies and giving rise to Mn-Mn connectivity, with a 'bow-tie' like arrangement. The pink and purple spheres and squares represent the Mn^{4+} ions and MnO_6 octahedra on the Mn1 and Mn2 crystallographic sites respectively. The teal spheres represent the Ca^{2+} ions and the red spheres the oxygen ions (Colour online).

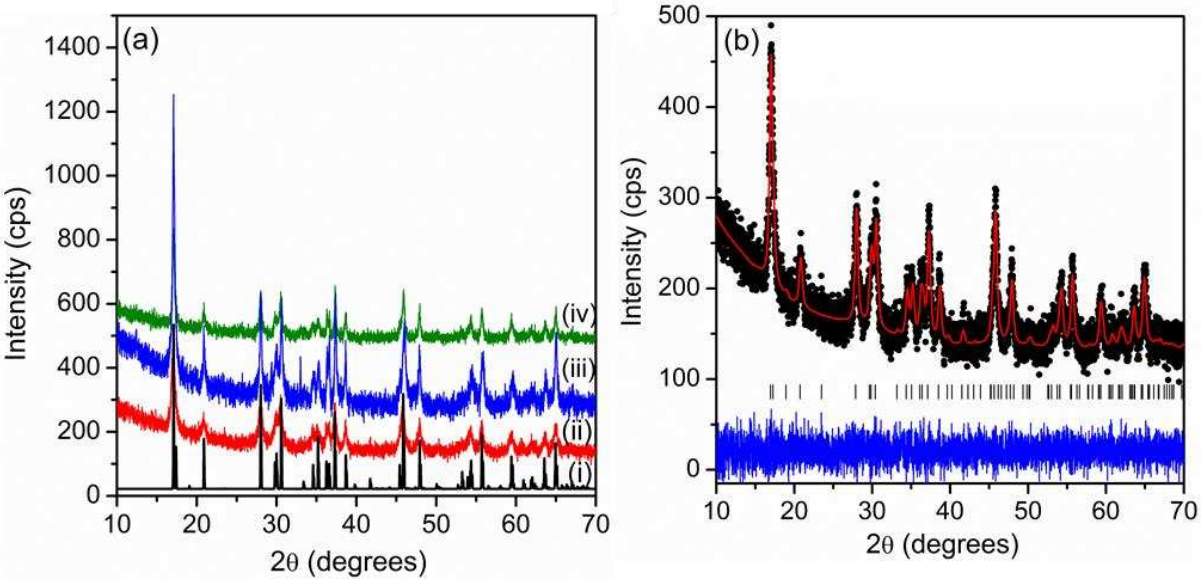

Figure 2: (a) Powder X-ray diffraction patterns for $Ca_2Mn_3O_8$ (i) showing the expected peak profile generated from the model proposed by Ansell et al.[12] and for materials prepared using (ii) sol-gel, (iii) hydrothermal and (iv) co-precipitation methods respectively (Note: an offset has been applied for comparative purposes) and (b) GSAS refinement profile showing the fit to the C2/m model for the sol-gel prepared material where the black circles represent the observed data, the red line represents the calculated model and the blue line represents the difference (Colour online).

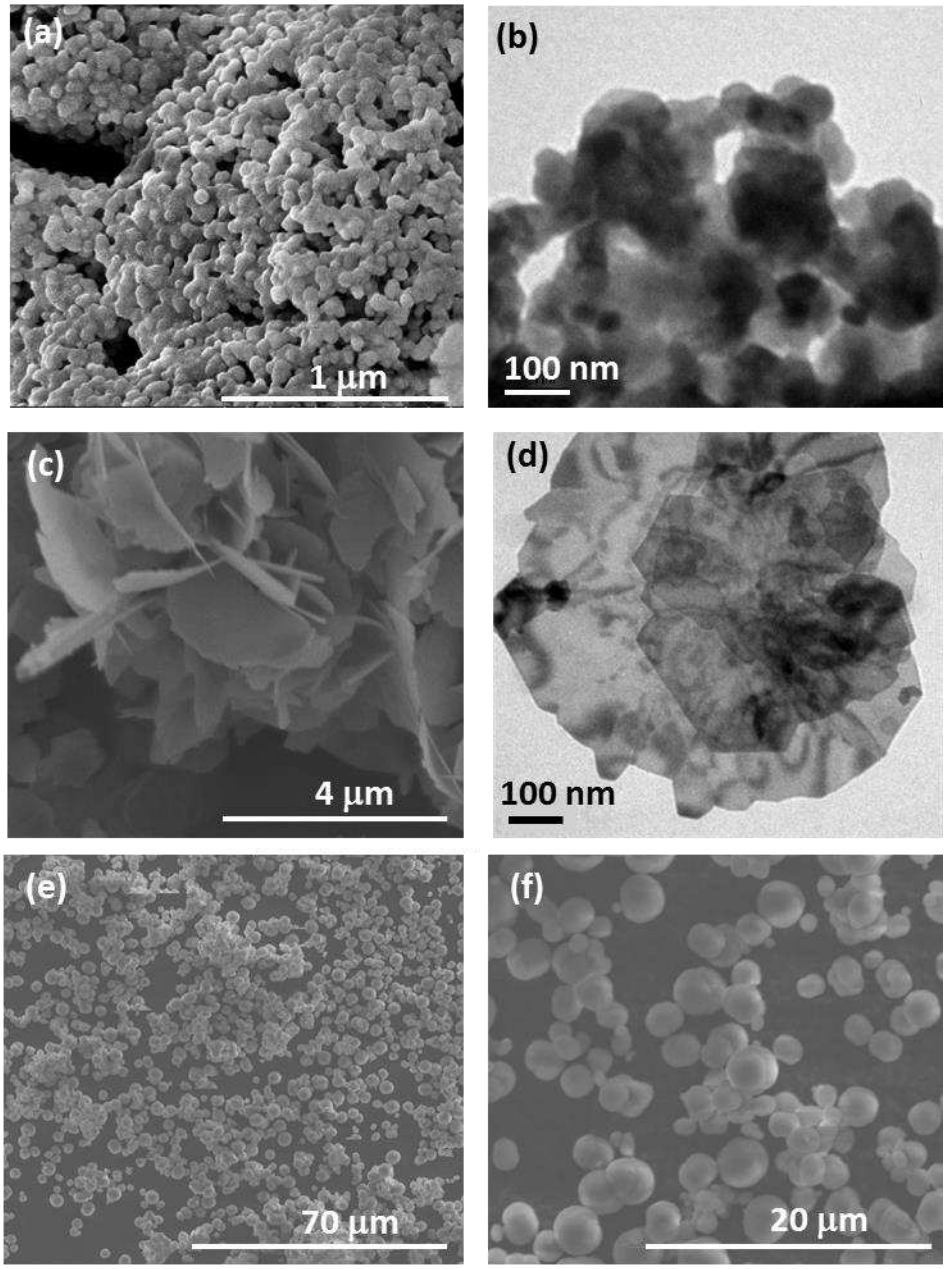

Figure 3: (a) FE-SEM and (b) TEM images collected for $Ca_2Mn_3O_8$ materials prepared using sol-gel synthesis, (c) SEM and (d) TEM images collected for $Ca_2Mn_3O_8$ materials prepared from hydrothermal synthesis and (e) and (f) SEM images collected for $Ca_2Mn_3O_8$ prepared using co-precipitation methods.

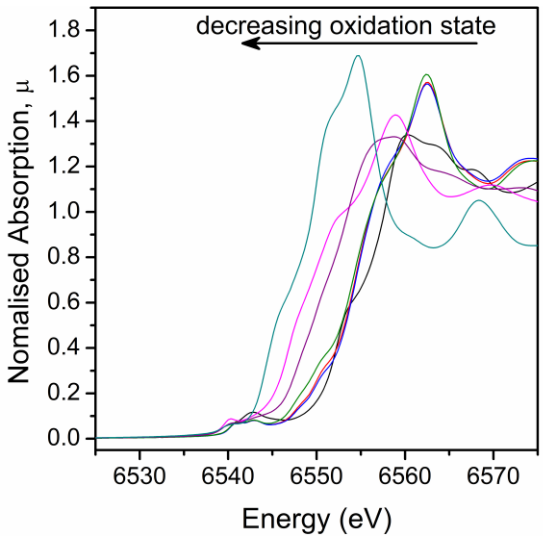

Figure 4: Normalised Mn K-edge XANES spectra showing the edge position of $Ca_2Mn_3O_8$ materials prepared by sol-gel (red), co-precipitation (blue) and hydrothermal (green) methods are consistent with MnO_2 (black) and thus an oxidation state of +4 in comparison with Mn_3O_4 (magenta), Mn_2O_3 (purple) and MnO (dark cyan). Note: all $Ca_2Mn_3O_8$ materials overlay further confirming the structural similarities in these materials. (An expanded energy range is shown in the ESI).†

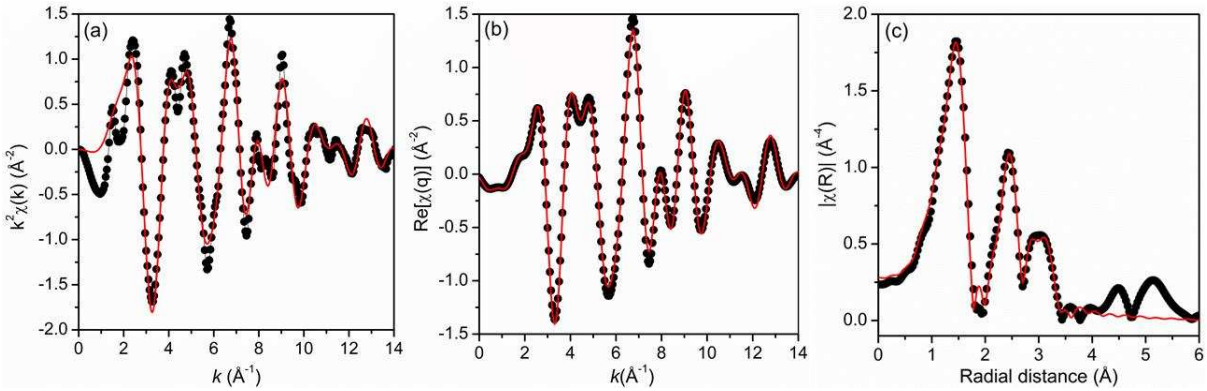

Figure 5: EXAFS spectra for the Sol-Gel prepared $Ca_2Mn_3O_8$ material where the black circles represent the observed data and the red line represents the fit. Fits are shown in (a) reciprocal (k) space, (b) q-space and (c) the real component of the EXAFS Fourier transform in real space (R).

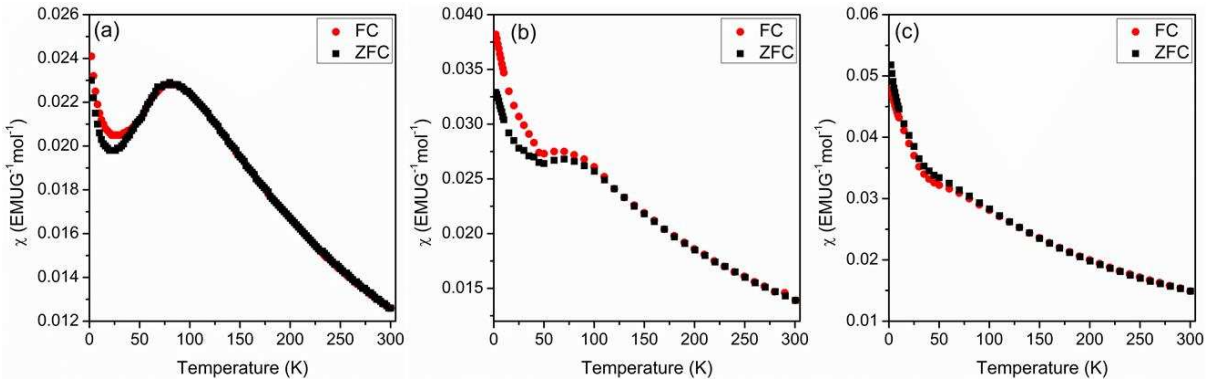

Figure 6: Zero field cooled (ZFC) and field cooled (FC) data collected in an applied field of 0.1 T for $Ca_2Mn_3O_8$ prepared by (a) co-precipitation, (b) sol-gel and (c) hydrothermal methods showing an antiferromagnetic phase transition, T_N, at approximately 50 K. Note: this is less pronounced in the materials prepared by hydrothermal synthesis.

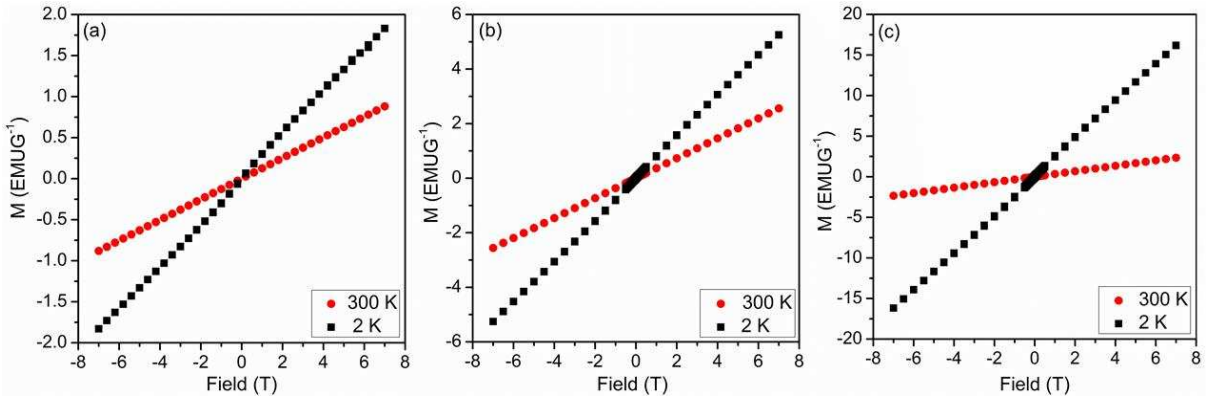

Figure 7: Field dependent data collected at temperatures of 2 K (red) and 300 K (black) for $Ca_2Mn_3O_8$ materials prepared by (a) co-precipitation, (b) sol-gel and (c) hydrothermal methods.